Redistribution of Terbium Ions Across Acetylcholine Receptor-Enriched Membranes Induced by Agonist Desensitization

Thomas E. Lee,[†] Anthony R. Chuang,[‡] Matthew S. Marek,[§] Sebastian Doniach,[¶] and Robert H. Fairclough[‖*]
[†]Department of Information Technology, Gilead Sciences, Foster City, California; [‡]Drexel University School of Medicine, Philadelphia, Pennsylvania; [§]Cellular and Molecular Biology Program, University of Michigan Medical School, Ann Arbor, Michigan; [¶]Departments of Physics and Applied Physics, Stanford University, Palo Alto, California; and [‖]Department of Neurology, University of California, Davis, Davis, California

ABSTRACT Using small-angle x-ray diffraction from centrifugally oriented acetylcholine receptor (AChR) enriched membranes coupled with anomalous scattering from terbium ions (Tb^{3+}) titrated into presumed Ca^{2+} binding sites, we have mapped the distribution of Tb^{3+} perpendicular to the membrane plane using a heavy atom refinement algorithm. We have compared the distribution of Tb^{3+} in the closed resting state with that in the carbamylcholine-desensitized state. In the closed resting state we find 45 Tb^{3+} ions distributed in 10 narrow peaks perpendicular to the membrane plane. Applying the same refinement procedure to the data from carbamylcholine desensitized AChR we find 18 fewer Tb^{3+} ions in eight peaks, and slight rearrangements of Tb^{3+} density in the peaks near the ends of the AChR ion channel pore. These agonist dependent changes in the Tb^{3+} stoichiometry and distribution suggest a likely role for multivalent cations in stabilizing the different functional states of the AChR, and the changes in the Tb^{3+} distribution at the two ends of the pore suggest a potential role for multivalent cations in the gating of the ion channel.

INTRODUCTION

The *Torpedo* acetylcholine receptor, like its mammalian muscle cousins, is resident in postsynaptic membranes where it responds to the binding of two equivalents of acetylcholine (ACh) by briefly (~ms) opening a cation selective pore. Through the open pore Na^+ and Ca^{2+} ions move down their electro-chemical gradients from the outside to the inside of the cell, depolarizing the postsynaptic membrane potential. Not only does Ca^{2+} pass through the open ion channel pore (1,2), but it also binds to the AChR resulting in altered channel properties. As external [Ca^{2+}] is titrated to a level just lower than physiological concentrations, one observes an increase in channel opening rate and a decrease in channel closing rate (1) with an overall potentiation of currents elicited by the binding of acetylcholine. When [Ca^{2+}] exceeds the physiological concentration, one observes an inhibition of agonist-induced Na^+ currents (1,2).

Using a nicotinic α7:5-hydroxytryptamine receptor (5-HT_3) chimeric receptor consisting of the homopentameric α7-AChR synaptic head covalently coupled to the transmembrane domain of the homopentameric serotonergic $5HT_3$, Galzi et al. (3) studied the Ca^{2+} potentiation effect. The homopentameric chimera $Na^+(K^+)$ currents are Ca^{2+} sensitive unlike those in the Ca^{2+} insensitive and Ca^{2+} impermeable 5-HT_3 receptor. The authors localized the Ca^{2+} potentiation to amino acids 161–172 of the α7-sequence with primary roles played by D163 and E172. These two amino acids are conserved in the *Torpedo* α, γ, and δ subunits, but not in the β subunit.

Homologous to α7 D163 in the *Torpedo* δ subunit is D180, which has been localized within 9 Å of α192/193 at an ACh-binding site of the *Torpedo* AChR (4). Mutation of the *Torpedo* δ D180 to N weakens the affinity of the neurotransmitter by a factor of 100 (4). In the ACh binding protein, for which an atomic resolution structure is available, the homolog to α7 D163 is D161, whose COO^- group is in direct contact with a Ca^{2+} ion in the refined structure (5).

Apart from the potentiation of agonist-induced currents by Ca^{2+}, the *Torpedo* AChR bathed in physiological Na^+ and Ca^{2+} releases four to six Ca^{2+} ions per receptor on binding ACh (6). Taken together, the aforementioned results indicate the presence of two or three regions of the AChR where Ca^{2+} interacts with the AChR to mediate functional effects.

In a previous study, we used Tb^{3+} to probe Ca^{2+} binding sites on AChR enriched membranes (7). The membranes treated with 50 μM Tb^{3+} were oriented in a centrifugal field, and the samples irradiated at two x-ray energies selected to tune the contribution of Tb^{3+} into and out of the small-angle x-ray meridional diffraction pattern. The difference between the diffracted x-ray amplitudes at the two x-ray energies was used with heavy atom refinement to determine the location and the amount of Tb^{3+} at each coordinate along an axis perpendicular to the plane of the bilayer. In this manner we identified six narrow clusters of Tb^{3+} density with a total of 45–47 Tb^{3+} ions localized in these regions along an axis perpendicular to the membrane plane (7). In this previous study, the Tb^{3+} stoichiometry was determined by the relative magnitude of the refined anomalous signal as well as spectroscopically with a Scatchard analysis of the depletion of Tb^{3+} from solution by the Tb^{3+} binding to AChR enriched membranes, and both indicated 45–47 Tb^{3+}bound/AChR.

The current study returns to compare the distribution of Tb^{3+} bound to a sample of AChR-enriched membranes desensitized with 20 μM carbamylcholine with that of the

Submitted November 4, 2007, and accepted for publication August 20, 2008.

*Correspondence: rhfairclough@ucdavis.edu

Editor: Jill Trewhella.

0006-3495/09/04/2637/11 $2.00

doi: 10.1016/j.bpj.2008.08.006

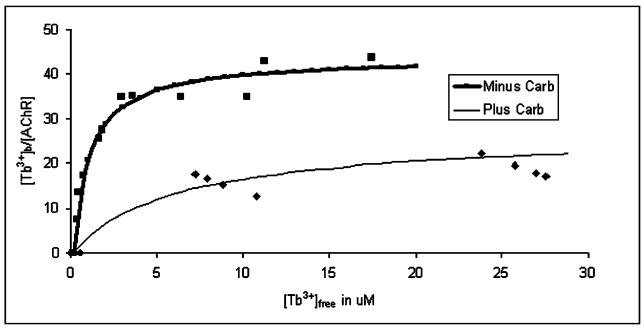

FIGURE 1 Tb^{3+} titration of 0.50 μM closed resting state AChR-enriched membranes (*top line*) and of 0.73 μM AChR-enriched membranes desensitized with 20 μM carbamylcholine (*bottom line*). The binding data were analyzed as described in Methods with the two fits (− and +carbamylcholine, respectively) of the parameters yielding $(D - A) = 44.0$ and 27.8; $C = 0.88$ and 6.1 μM; $B = 0.98$ and 0.94. The determinations of the saturating amounts of Tb^{3+}/AChR are quite close to those we observe in the x-ray analysis for both samples.

sample of membranes in the closed resting state reanalyzed with a new heavy atom refinement algorithm, with a slightly larger refinement window used for both data sets. This is an attempt to distinguish regions of Tb^{3+} density that change on agonist desensitization of the AChR. The titration of closed resting state AChR-enriched membranes and then of carbamylcholine-desensitized membranes indicates 44–45 and 27–28 bound Tb^{3+}/AChR, respectively. Refinement of the two x-ray data sets shows 8–10 narrow peaks of Tb^{3+} density in both samples with 45 Tb^{3+} and 27 Tb^{3+} bound in the closed resting and desensitized states respectively. Agonist-induced losses of roughly two or more Tb^{3+} ions occur in five of the 10 Tb^{3+} peaks, and slight redistribution of Tb^{3+} density occurs in two of the other regions. These last two regions are aligned at the ends of the level of the ion channel pore near the rings of carboxylates identified by Imoto et al. (8) and the gate mapped by Karlin and colleagues and summarized in Wilson and Karlin (9). The changes we observe in Tb^{3+} density in the regions of the agonist binding sites and at the ends of the ion channel pore suggest a role for multivalent cations in the stabilizing the different functional states of the AChR, a role for them mediating molecular transitions between states, and a role for them linking events in the agonist binding domain to those in the ion channel domain.

METHODS

Preparation of AChR enriched membranes for titration and x-ray diffraction

Alkali-stripped ACh receptor-enriched membrane vesicles (10) were prepared from frozen *Torpedo* electric organ as described in Fairclough et al. (7). The AChR-enriched fractions at 3 mg of protein/mL from this prep were stored in 10 mM phosphate buffer pH 7.8 with 1 mM EGTA, 1 mM EDTA, and 0.02% (w/v) NaN_3 (buffer A) at 4°C. To prepare samples for Tb^{3+} titration, the AChR-enriched membranes were removed from the chelating agents in buffer A by 25-fold dilution in 10 mM PIPES buffer pH 6.8 and pelleted for 30 min at 20,000 rpm in an SW65 rotor or 10 min at 20 psi in an airfuge. The pellets were then resuspended in 10 mM PIPES buffer pH 6.8 and diluted to 0.50 μM and 0.73 μM AChR in a total volume of 36 μL of 10 mM PIPES pH 6.8, 100 mM NaCl, without and with 20 μM carbamylcholine, respectively, and titrated with 0–80 μM Tb^{3+}. Membranes were spun in an airfuge for 10 min at 20 psi in a 30° angle rotor after which 4 μL of supernatant was assayed in 2.0 mL of aqueous solution of 10 μM dipicolinic acid (DPA) and analyzed fluorometrically for Tb^{3+} using either a Perkin-Elmer (Norwalk, CT) MPF-44A spectrofluorometer or an SLM 4800C spectrofluorometer (11). The DPA-Tb^{3+} assay was used to measure the initial Tb^{3+} concentration as well as that of the supernatant. The difference was taken to reflect the amount bound to the pelleted membranes. The $[Tb^{3+}]_b$/[AChR] versus $[Tb^{3+}]_f$ data were analyzed using $y = (A - D)/[1 + (x/C)^B] + D$ where $y = [Tb^{3+}]_b/[AChR]$; $x = [Tb^{3+}]_{free}$; $C = [Tb^{3+}]_f$ at 1/2 $(D - A)$; and B ~1.0, the Hill coefficient, and the parameters determined by nonlinear least squares fit of A, B, C, and D with DeltaGraph Red Rock Software (Salt Lake City, UT) and presented in Fig. 1.

For each sample to be x rayed, 150 μL (0.45 mg protein) of the membranes were diluted to 5.0 mL in 10 mM PIPES buffer pH 6.8 and pelleted in a Beckman (Palo Alto, CA) SW 65 rotor at 35 K rpm for 45 min. The pellet was suspended in 100 μL 10 mM PIPES buffer. This was diluted to 3.6 mL of 10 mM-PIPES pH 6.8, 100 mM NaCl, 50 μM Tb^{3+} ± 20 μM carbamylcholine, and spun at 50 K rpm for 22 H in the SW65 rotor fitted with a membrane funnel and sample cell holder with Mylar windows (12). After centrifugation the supernatant was removed by pipette, the top of the pellet was dried of excess buffer with a tightly rolled Kimwipe (Kimberly-Clark, Roswell, GA), and the cell was sealed with silicone high vacuum grease (Dow Corning, Midland, MI), and the sealed sample cell disc was stored at 4°C until placed in the small-angle x-ray camera.

Small-angle x-ray diffraction experiments with anomalous scattering

Small-angle x-ray diffraction experiments were conducted at the Stanford Synchrotron Radiation Laboratory as described previously (7). Centrifugally oriented membranes were maintained at 4–6°C on the camera with a Lauda water bath to help preserve membrane orientation. Meridional diffraction intensities were recorded with a linear position-sensitive detector by aligning the membrane sample with the average orientation of the membrane planes parallel to the x-ray beam and perpendicular to the wire of the linear detector. Equatorial intensities were subsequently recorded for the same sample by rotating the sample 90° about the x-ray beam so that the orientation of the membrane planes was parallel to the wire of the detector. Both meridional and equatorial data were acquired using a Gabriel (13) linear position-sensitive proportional counter with delay line encoding (14,15). The raw scattering intensity profiles versus the scattering variable, s, were calculated as described in Fairclough et al. (7) by averaging the intensities from the two sides of the beam stop and correcting the meridional signal at each energy for Tb^{3+} x-ray fluorescence. The meridional and equatorial profiles were collected at five x-ray energies: 7505, 7510, 7515, 7518, and 7525 eV. However, only the 7505 and 7515 eV data in each case (±carbamylcholine) were used in the anomalous scattering analysis of Tb^{3+} location relative to the phosphate headgroups of the lipid bilayer. The equatorial intensity profile was used as a guide to obtain the diffuse background scattering to subtract from the raw meridional profile to obtain the oriented meridional intensity profile at each of the two energies. For carbamylcholine treated and untreated membranes, the meridional intensity profile at 7515 eV was subtracted from that at 7505 eV respectively to arrive at the oriented anomalous difference profiles in the presence and absence of carbamylcholine. These are presented in Fig. 2.

Conversion of anomalous intensity differences to amplitude differences

For the membranes not treated with carbamylcholine, the oriented meridional intensities as a function of s are corrected for the finite size of the

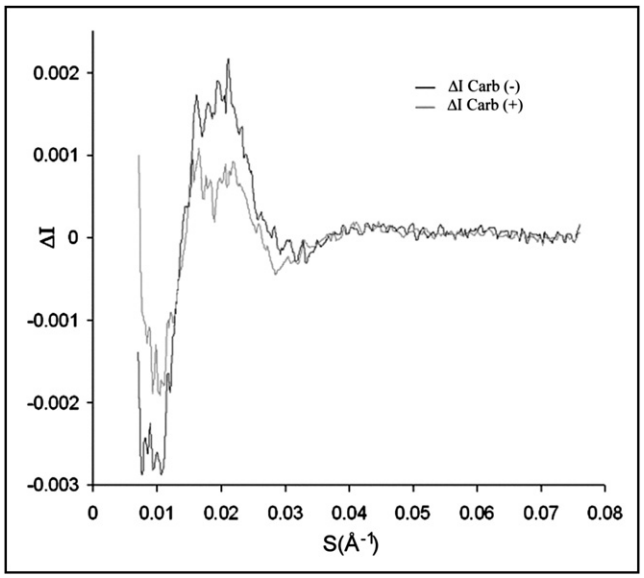

FIGURE 2 $\Delta I(s) = I_{7505}(s) - I_{7515}(s)$ meridional diffraction difference intensity data for membranes without and with 20 μM carbamylcholine as a function of s in $Å^{-1}$.

beam (bhw) and the membrane orientation factor (tanθ) that accounts for the smaller fraction of membranes oriented to diffract x rays to large values of s as described in Fairclough et al. (7) in which $I_{corrected}(s) = I_{raw}(s)[(bhw + s \bullet \tan\theta)/bhw]^2$. In this study bhw was 0.0018 $Å^{-1}$, and $\tan\theta = 0.141$. The corrected intensities are then used to calculate the observed amplitudes, $F_{o\text{-}7505}(s)$ and $F_{o\text{-}7515}(s)$, by extracting the square root of the corrected intensities at each value of s. A final scaling of the amplitudes was applied by matching the integrated area under the pattern to the area under the Fourier transform of the scaled membrane electron density profile presented by Klymkowsky and Stroud (16).

For the membranes treated with carbamylcholine, the only data that is accessible is a hard copy of the $\Delta I_{7505\text{–}7515}(s)$ versus s before correction for the finite beam size and membrane orientation correction and final scaling. (The original uncorrected $I_{7505}(s)$ and $I_{7515}(s)$ were not retrievable from the tape on which these files were saved.) To arrive at the corrected amplitudes, $F(s)$ versus s, a slightly more involved data reduction was used. The $\Delta I(s)$ of the carbamylcholine treated membranes was added to the $I_{7515}(s)$ calculated from $F_{o\text{-}7515}(s)$ of the sample untreated with carbamylcholine to give the $I_{7505}(s)$ for the sample treated with carbamylcholine. Each of these intensities is then corrected for the finite beam width and membrane orientation and final scaling using the same values for these factors as was used for the sample without carbamylcholine treatment. The use of the $F_{7515}(s)$ from the membranes not treated with carbamylcholine for that from membranes treated with carbamylcholine is justified by the lack of observed carb induced structural change of the AChR along the axis $\perp$ to the bilayer in an electron microscopic study (17) as well as the small calculated contribution to $F_{7515}(s)$ of the carb induced change in Tb/AChR ratio (see Fig. S1 in the Supporting Material for a flow chart of this data treatment and the justification for the substitutions we make).

Refinement of the Tb^{3+} ion distribution

The refinement of the Tb^{3+} distribution builds on the observables at the two x-ray energies, 7505 and 7515 eV: $F_{o\text{-}7505}(s)$ and $F_{o\text{-}7515}(s)$. Tb^{3+} contributes more scattering power at 7505 eV than at 7515eV, and because the sample remains the same, the diffraction data collected at these two energies provides the raw data for an isomorphous "heavy atom refinement" exercise. Using the $F_{o\text{-}7515}(s)$ (Fig. 3 *a*) and the constrained iterative refinement procedure of Agard and Stroud (18), a refined electron density in a 260 Å

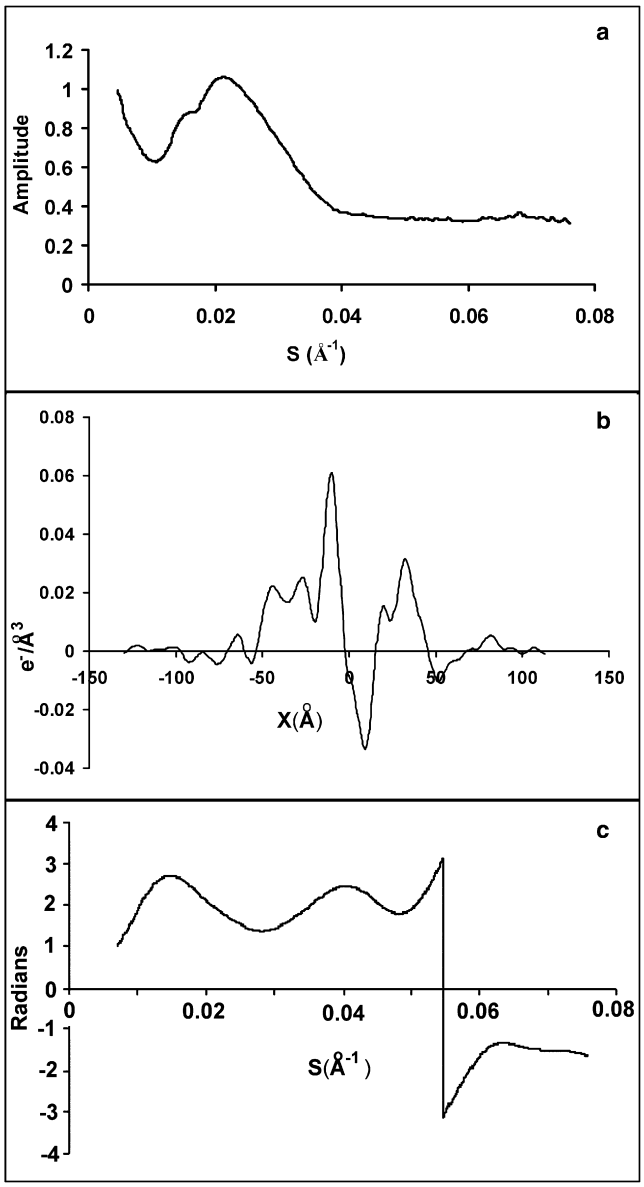

FIGURE 3 (*a*) $F_{o\text{-}7515}(s)$ measured meridional diffraction amplitude versus s in $Å^{-1}$. (*b*) Electron density distribution across the membrane lipid bilayer relative to water, generated from constrained iterative refinement of $F_{o\text{-}7515}(s)$ data presented in *a*. (*c*) Phases, $\varphi(s)$, produced by the back transform of the calculated electron density presented in *b*, and used in Eq. 1 to generate the complex amplitude of the membrane $F_{r\text{-}7515}(s)$ and $F_{i\text{-}7515}(s)$ used in the refinement scheme to obtain the positions and amplitude of the Gaussians as described in Methods and outlined in Fig. S2.

window across the membrane is determined (Fig. 3 *b*). This is back transformed to compute the phases, $\varphi(s)$ (Fig. 3 *c*), which are combined with $F_{o\text{-}7515}(s)$ to calculate the complex amplitudes at 7515 using Eq. 1: $F_{r\text{-}7515}(s)$ and $F_{i\text{-}7515}(s)$.

$$F_{r-7515}(s) = F_{o-7515}(s) \times \cos\varphi(s)$$
$$F_{i-7515}(s) = F_{o-7515}(s) \times \sin\varphi(s). \quad (1)$$

The Tb^{3+} distribution refinement begins with a random distribution of 45 Tb^{3+} ions in a 220 Å window along an axis, X, perpendicular to the bilayer plane. Each Tb^{3+} ion is modeled as a Gaussian function centered

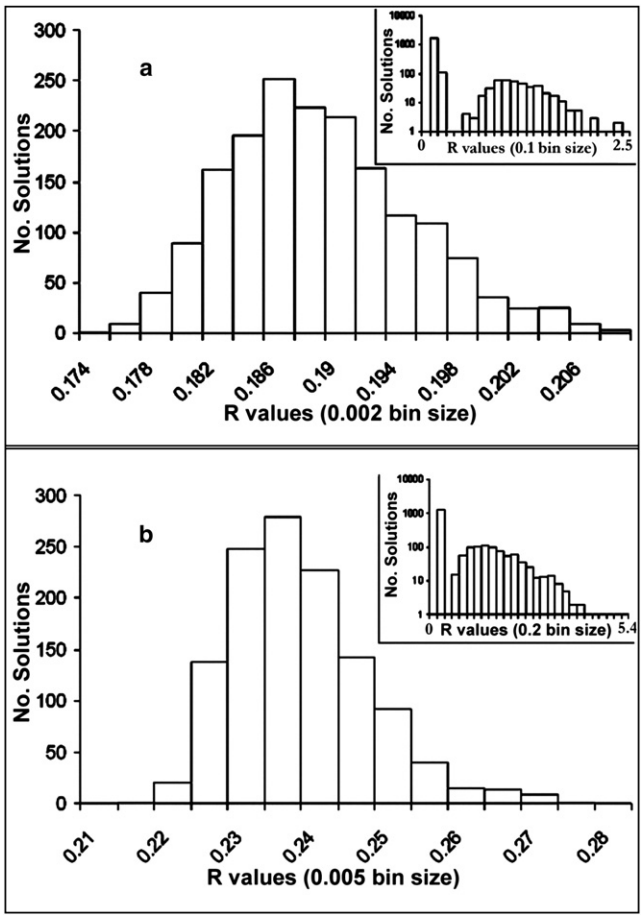

FIGURE 4 (*a*) Distribution of *R*-factors for ~2000 Tb^{3+} distribution solutions for membranes in the closed resting state. (*b*) Distribution of *R*-factors for ~1800 Tb^{3+} distribution solutions for carbamylcholine-desensitized membranes.

at X_i (with $i = 1,\ldots,45$) with amplitude, *A*, and the temperature factor, *B*, fixed at 78.96Å^2. The refinement was carried out in a 220 Å window slightly smaller than the 260 Å window used for the constrained iterative refinement of the membrane and yet larger than the expected dimension across the membrane from the AChR structural model from Unwin's electron microscopic study (19). This window was chosen as the smallest that enabled the prediction of most of the major features of the anomalous amplitude differences (see Fig. 5).

The initial Tb^{3+} distribution is used to calculate the contribution of the Tb^{3+} ions to the complex amplitude at 7505 eV using Eqs. 2 and 3:

$$G_r(s) = \sum_n A \times e^{-(B\times s^2/4.0)} \times \cos(2\times\pi\times s\times X_n)$$
$$G_i(s) = \sum_n A \times e^{-(B\times s^2/4.0)} \times \sin(2\times\pi\times s\times X_n). \quad (2)$$

These complex amplitudes are combined with those from the refined 7515 eV membrane diffraction data using Eq. 3 to arrive at an estimate of the amplitude at 7505 eV.

$$F_{c-7505}(s) = \sqrt{(F_{r-7515}(s)+G_r(s))^2+(F_{i-7515}(s)+G_i(s))^2}. \quad (3)$$

The positions of the Gaussians are adjusted iteratively along with the amplitude, *A*, to minimize the difference between the calculated amplitude at 7505eV, $F_{c\text{-}7505}(s)$, and the observed amplitude at 7505eV, $F_{o\text{-}7505}(s)$. This difference is evaluated by calculating the *R*-factor defined by Eq. 4:

$$R = \sum_s (F_{c-7505}(s) - F_{o-7505}(s))^2 / \sum_s (F_{o-7505}(s) - F_{o-7515}(s))^2. \quad (4)$$

When no further adjustment of the positions and amplitude result in a decrease in the value of *R*, the final positions (the X_i), the amplitude, and the *R*-factor constitute a "solution" that is saved to a database as a Tb^{3+} distribution solution. This process, beginning with a different random distribution of 45 Gaussians, is repeated until several thousand Tb^{3+} distribution solutions are accumulated (Fig. 4).

This simple algorithm, summarized in Fig. S2, has the advantage of being easily distributed across many computers, where each computer independently follows the algorithm outlined in the flow chart. Software written in the programming language C# allows this process to run as a background task on desktop computers running the Windows operating system. Tb^{3+} distribution solutions are accumulated in a SQL Server 2000 database (Microsoft Software, Redmond, WA).

The five Tb^{3+} distribution solutions with the lowest *R*-factors were used with Eq. 5 and $m = 1,\ldots,5$ to calculate an average Tb^{3+} distribution solution with the *R*-factor lowered by an additional 1%–2%:

$$G_r(s) = \left(\sum_{nm} A_m \times e^{-(B\times s^2/4.0)} \times \cos(2\times\pi\times s\times X_{nm})\right)/5$$
$$G_i(s) = \left(\sum_{nm} A_m \times e^{-(B\times s^2/4.0)} \times \sin(2\times\pi\times s\times X_{nm})\right)/5. \quad (5)$$

For a visual assessment of how well the refined Tb^{3+} distribution predicts the observed anomalous scattering data, we compare the observed anomalous amplitude differences $\Delta F_o(s) = F_{o\text{-}7505}(s) - F_{o\text{-}7515}(s)$ with those calculated from $F_{c\text{-}7505}(s) - F_{o\text{-}7515}(s)$ and present them in Fig. 5, *a* and *b* for membranes untreated and treated with carbamylcholine. The refined distributions along with the averages themselves are presented in Fig. 6, *a* and *b*.

Determination of the Tb^{3+}/AChR stoichiometry

The areas under the average curves in Fig. 6, *a* and *b*, were used along with the area under Fig. 3 *b* to determine the Tb^{3+}/AChR stoichiometry in the two samples (see Eq. 7). Equation 6a expresses the relationship between the number of Tb^{3+} ions (N_{Tb}) in the irradiated sample volume (*V*) and the electron density profiles (Fig. 6, *a* and *b*), where seven electrons per Tb^{3+} ion contribute to the anomalous difference. Similarly, Eq. 6b expresses the relationship between the electron density profile of AChR membranes relative to water (Fig. 3 *b*) and the number of AChR (M_{AChR}) in the same volume, where $Ne_{AChR+Tb}$ is the number of electrons in AChR with bound Tb^{3+} ions, and Ne_{H_2O} is the number of electrons in water displaced by AChR.

$$(7 \times N_{Tb}/V) = k \sum_{z=-120}^{z=100} \Delta\rho_{7505-7515}, \quad (6a)$$

$$(Ne_{AChR+Tb} - Ne_{H_2O}) \times M_{AChR}/V = k \sum_{z=-120}^{z=100} \Delta\rho_{AChR\text{-}H_2O}. \quad (6b)$$

Dividing Eq. 6a by Eq. 6b and solving for N_{Tb}/M_{AChR} the number of Tb^{3+} ions per receptor, one finds (Eq. 7):

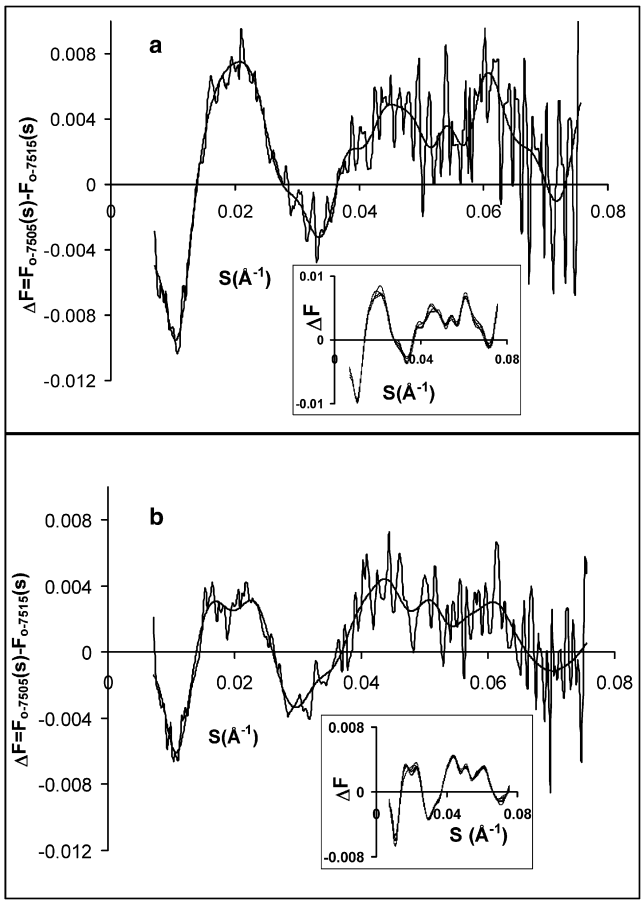

FIGURE 5 (*a*) Anomalous difference amplitude, $\Delta F(s)$ from membranes in the closed resting state (*noisy*), compared with average of the five best refined solutions (*smooth*) plotted as $F_{c\text{-}7505}(s) - F_{o\text{-}7515}(s)$. Calculated curves from individual refined solutions, which formed the average, are presented in the inset. (*b*) Anomalous difference amplitude, $\Delta F(s)$ from AChR enriched membranes in carbamylcholine-desensitized state (*noisy*), compared with the average of five best refined solutions (*smooth*) plotted as $F_{c\text{-}7505}(s) - F_{o\text{-}7515}(s)$. Individual refined solutions, which formed the average, are presented in the inset.

$$N_{\mathrm{Tb/AChR}} = \frac{N_{\mathrm{Tb}}}{M_{\mathrm{AChR}}} = \frac{(Ne_{\mathrm{AChR+Tb}} - Ne_{\mathrm{H_2O}})}{7} \times \frac{\sum_{z=-120}^{z=100} \Delta\rho_{7505-7515}}{\sum_{z=-120}^{z=100} \Delta\rho_{\mathrm{AChR\text{-}H_2O}}}. \quad (7)$$

For purposes of calculating the difference between the number of electrons in the AChR/Tb complex and the number of electrons in the displaced water, we have estimated the number of Tb^{3+} ions per receptor ($N_{\mathrm{Tb/AChR}}$) in the closed resting state to be 45 Tb/AChR. The number calculated using Eq. 7 turns out to be 45. Using the ratio of anomalous electron density in the carbamylcholine treated sample to that in the nontreated sample along with the 45 Tb, we find 27 Tb/AChR in the carbamylcholine sample. Table 1 summarizes the values used in these calculations. The total number of Tb^{3+} ions is then distributed into the narrow domains by the fractional area of each domain and summarized in Table 2. We have not included several minor

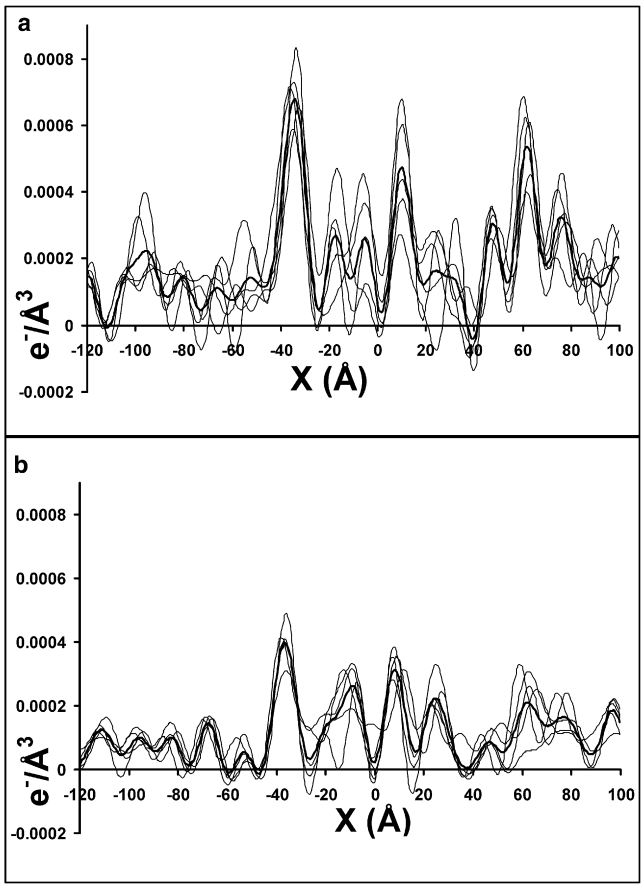

FIGURE 6 (*a*) Five best refinement solutions (*light lines*) and average of five solutions (*darker line*) for data without carbamylcholine plotted in real space. *Y* axis is electron density of Tb^{3+} relative to water. (*b*) Five best refinement solutions (*light lines*) and average of five solutions (*darker line*) for data with carbamylcholine plotted in real space. *Y* axis is electron density of Tb^{3+} relative to water.

domains in Table 7, which accounts for the apparent shortfall in total Tb^{3+} in the table. However, we have included some of these small domains in Fig. 8 and not included the 4–5 Tb^{3+} in peak 1 so that the total illustrated in Fig. 8 is 40 bound Tb^{3+} ions.

RESULTS

Changes in Tb^{3+} binding on carbamylcholine desensitization

AChR-enriched membranes depleted of Ca^{2+} ions by storage in 1 mM EGTA, 1 mM EDTA phosphate buffer pH 7.8, then removed from the low ionic strength chelating phosphate buffer and suspended in PIPES buffer pH 6.8, 100 mM NaCl at 0.5 μM AChR, and finally titrated with Tb^{3+} ions, show 44–45 available Tb^{3+} sites/AChR with a dissociation constant of 0.88 μM as shown in Fig. 1 (*top line*), a reworking of the data from Fairclough et al. (7). A similar titration carried out on AChR-enriched membranes in the presence of 20 μM carbamylcholine produced only 27–28 available sites/AChR with a single dissociation constant of 6.1 μM as shown in Fig. 1 (*bottom line*).

TABLE 1 Integrated electron densities and numbers for finding Tb^{3+}/AChR stoichiometry

Quantity	Value
$\sum_{z=-120}^{z=100} \Delta\rho_{\text{AChR-H}_2\text{O}}$	1.291, from Fig. 2 *b*
$\sum_{z=-120}^{z=100} \Delta\rho_{7505-7515}$	0.04159, from Fig. 6 *a* (closed resting state) 0.02541, from Fig. 6 *b* (carbamylcholine desensitized state)
$(Ne_{\text{AChR+Tb}} - Ne_{\text{H}_2\text{O}})$	9890, where the number of Tb^{3+} electrons was $45 \times 62 = 2790$, the number of electrons from AChR was $0.5 \times (268{,}000) = 134{,}000$, and the number of electrons from displaced water (126,900) was the volume of a receptor times (0.334 e/Å^3) with the volume of AChR taken as 380,000 Å^3 (16) and estimates based on the Unwin structural model of the AChR (19)

The anomalous amplitude signal

AChR-enriched membranes treated in a similar manner as above in the presence and absence of 20 μM carbamylcholine and 50 μM Tb^{3+} are centrifugally oriented, and the prepared samples used to diffract x rays into the small-angle range ($0.007\ \text{Å}^{-1} < S < 0.08\ \text{Å}^{-1}$) at the two x-ray energies that are studied in this report: 7505 and 7515 eV. The diffracted intensity data sets at the two energies are converted to the respective amplitudes, $F_{\text{o-7505}}(s)$ and $F_{\text{o-7515}}(s)$, for both carbamylcholine-treated and untreated samples. For each sample the two amplitude data sets are quite similar. However, by subtracting 7515 eV amplitudes from 7505eV amplitudes, i.e., $F_{\text{o-7505}}(s) - F_{\text{o-7515}}(s)$, one detects an anomalous difference ''wave'' that is dependent on the Tb^{3+} ion distribution (7). The differences between the 7505eV and 7515eV amplitudes (Fig. 5) serve as the basis for refining the Tb^{3+} distribution in these two samples.

Application of the refinement scheme

The refinement scheme described in the Methods used four Pentium computers over a 1-month time period. We refined the preexponential amplitude factor and the positions of 45 randomly positioned Gaussian functions in a 220 Å window for 2000 initial Tb^{3+} ion distributions constrained by the anomalous diffraction data recorded in the absence of carbamylcholine. The refinements generated Tb^{3+} distribution solutions with minimum *R*-factors ranging from 0.1747 to 2.5 displayed in Fig. 4 *a*. Over a similar time period the refinement of the amplitude and 45 Gaussian positions for the anomalous data from the sample treated with carbamylcholine generated 1800 Tb^{3+} ion distribution solutions with *R*-factors ranging from 0.2187 to 4.200 displayed in Fig. 4 *b*. In Fig. 4 one also sees the solutions with the lowest *R*-factors are bunched in a rather narrow range: 0.17–0.21 for the minus and 0.21–0.28 for the plus carbamylcholine treated samples, respectively.

TABLE 2 Refined peak characteristics

Peak	Position (Å)	No. of Tb −carb (+carb)	FWHM (Å)
1	−95.0	4.8 ± 0.7 (3.0 ± 0.5)	16.9
2	−35.0	9.3 ± 1.3 (4.8 ± 0.5)	11.2
3	−16.5*	2.9 ± 1.2	10.0
4	−4.5* (*−8.0*)	2.5 ± 1.5 (*4.5 ± 1.2*)	10.0 (*13*)
5	9.0	5.3 ± 1.6 (3.5 ± 0.6)	9.5
6	25* (*26*)	2.0 ± 1.0 (*3.0 ± 0.6*)	7 (*10*)
7	32*	1.0 ± 0.7	6
8	48.0	2.8 ± 0.3 (1.0 ± 0.4)	8.0
9	62.0	6.3 ± 1.0 (3.0 ± 1.1)	10.0
10	76.0	4.3 ± 0.6 (2.5 ± 0.4)	10.0

*Two adjacent peaks in the absence of carbamylcholine seem to coalesce into a single peak in the presence of carbamylcholine (*italic*). Overall Tb^{3+}/AChR 45.1 ± 5.3 (*27.1 ± 2.2*); Δ = 18.0 ± 7.5 Tb.
FWMH, full width at half maximum.

The refined Tb^{3+} ion distributions

The five Tb^{3+} distribution solutions with the smallest *R*-factors are each used to predict the anomalous difference amplitudes, $F_{\text{c-7505}}(s) - F_{\text{o-7515}}(s)$, which are plotted with the observed difference in Fig. 5 *a*, *inset*, for membranes without carbamylcholine and in Fig. 5 *b*, *inset*, for membranes with carbamylcholine. In each case (±carbamylcholine) the five best distributions were averaged to produce a new distribution with improved *R*-factors of 0.1721 and 0.2149, respectively. The calculated amplitude differences for the average Tb^{3+} distributions overlay the experimentally observed differences for the − and +carbamylcholine treated samples in Fig. 5, *a* and *b*, respectively. The Tb^{3+} ion distributions themselves are presented in Fig. 6, *a* and *b*, respectively with the dark line being the average distribution in each case. Averaging more than the best five distributions did not produce an average distribution with an *R*-factor better than the individual solutions. The average distributions in Fig. 6, *a* and *b*, when integrated from 100 to −120 Å and compared with the integrated membrane distribution over the same interval from Fig. 2 *b*, show the stoichiometry of Tb^{3+}/AChR in the two samples of 45 and 27, respectively, for the carbamylcholine untreated and treated samples, respectively.

Fig. 7 presents the two average Tb^{3+} distributions along with the membrane electron density distribution perpendicular to the bilayer, aligned with the C_α trace of the Unwin structural model of the AChR ((19); PDB accession code 2BG9). The model is aligned by eye with the transmembrane helices of the AChR model centered between the two major peaks of electron density from the phosphate headgroups at −11 Å and +32 Å.

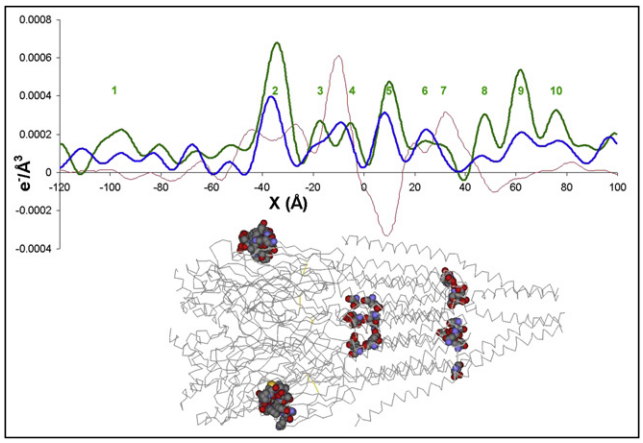

FIGURE 7 Electron density of membranes (×0.01) (*red*, from Fig. 3 *b*) relative to water along an axis, *X*, perpendicular to the bilayer plane of AChR-enriched membranes, and the average Tb^{3+} electron density distribution across the AChR-enriched membranes in the closed resting state (*green*, the average from Fig. 6 *a*) and in the carbamylcholine-desensitized state (*blue*, the average from Fig. 6 *b*). In the membrane electron density profile (*red curve*), the peaks at −10 and 35 Å locate the electron dense phosphate headgroups of the extracellular and cytoplasmic facing leaflets of the bilayer, respectively. Extracellular protein density extends to the left of the extracellular phosphates and the cytoplasmic protein density extends to the right of the cytoplasmic facing phosphate groups. Aligned with these profiles is the Cα trace of the 4 Å model of the AChR from Unwin (19). This model, presented for reference purposes, has the acetylcholine binding sites marked by the β-hairpin C-loops of the two α subunits (185–199) in CPK space-filling side-chains, and then the transmembrane extracellular, intermediate, and cytoplasmic Imoto rings (8), also highlighted in CPK space-filling format. The 10 refined peaks in the Tb^{3+} ion distribution of the closed resting state are numbered left to right and correspond to the peaks listed in Table 2.

Description of the Tb^{3+} distributions ±carbamylcholine

The Tb^{3+} distribution across membranes in the closed resting state (Fig. 7, *green curve*) consists of three major narrow (FWHM ~10 Å) peaks of > 5 Tb^{3+} ions in the 220 Å window and seven minor peaks of <5 Tb^{3+} ions each. The location and occupation of these peaks are summarized in Table 2. Referring to Fig. 7 and Table 2, the three major peaks fall in 1), the middle of the extracellular head at −35 Å; 2), the transmembrane domain at +9 Å; and 3), the cytoplasmic extension at +62 Å. Each of these groups retains ~50% of the bound Tb^{3+} ions in the carbamylcholine-desensitized state.

Among these major peaks, the one (peak 2 in Table 2) at −35 Å represents nine Tb^{3+} ions and maps to a location just a short distance closer to the bilayer than the agonist binding site (the two CPK space filling C-loops on the side of the AChR model). This region of the AChR seems to bind only five Tb^{3+} ions in the carbamylcholine-desensitized state. This peak seems to correlate in location on the AChR to the location of the five Ca^{2+} binding sites on the periphery of the ACh-binding protein (5), but with a nine Tb^{3+} stoichiometry likely includes additional sites on the wall of the vestibule.

Somewhat surprising among the major peaks is peak 5 with 5.3 Tb^{3+} ions centered at 9.0 Å. With these Tb^{3+} ions representing a total positive charge of 15, this group seems to be charge-balanced by only the three negatively charged carboxylates of the Imoto intermediate ring around the pore (8). This Tb^{3+} group presents an interesting dilemma: what is holding the multivalent cations at this location? In the desensitized state we find two less Tb^{3+} ions at this location.

The last of the major peaks (peak 9) is found at 62 Å with six Tb^{3+} ions in the resting state but only three in the desensitized state. This peak clearly lies in the cytoplasmic domain of the AChR with the amphipathic helix of each subunit the only structural motif displayed in the 4 Å model (19) with some 67–100 amino acids of each subunit not displayed. The amphipathic helices do provide potential chelating possibilities for this peak.

The minor peaks appear to be slightly broader than the major peaks with the one at −95 Å (peak 1) located surprisingly some 25 Å above the protein synaptic head of the AChR and representing 4.8 Tb^{3+} ions. Despite the Tb^{3+} density in this peak falling well above the top of the protein synaptic domain of the Unwin model (Fig. 7), desensitization of the AChR with carbamylcholine results in the binding of approximately two fewer Tb^{3+} ions in this cluster and the binding of one Tb^{3+} in several peaks (blue curve -120 Å $< X < -50$ Å) at the ''noise'' level of the experiment. A second dilemma thus arises: what is anchoring the Tb^{3+} ions at this location above the protein synaptic domain?

The minor Tb^{3+} cluster (peaks 3 and 4) between −20 and 0 Å maps to a location in the 4 Å model (19) near the synaptic side junction of the β-strand domain with the α-helical domain and the extracellular entrance to the ion channel pore. In the closed resting state, this cluster is bifurcated with two or three Tb^{3+} ions centered at −19 and at −4 Å. In the presence of carbamylcholine these two coalesce into a broad four to five Tb^{3+} group peaking at –10 Å. This group maps close to the Imoto extracellular ring and the carbonyl backbone of the intermediate ring of carboxylates (8). Another minor cluster (peaks 6 and 7) at 26 Å displays one to two Tb^{3+} ions in each of another bifurcated group in the closed resting state that in the desensitized state appear as a single peak of three Tb^{3+} ions at 26 Å. This group maps to a level at the cytoplasmic end of the ion channel pore corresponding to the Imoto cytoplasmic ring of carboxylates (8). The Tb^{3+} ions in the bifurcated groups in the resting state at either end of the pore seem to redistribute along the normal to the membrane on carbamylcholine desensitization.

The final two minor peaks (peaks 8 and 10) are centered at 48 and 76 Å in the cytoplasmic domain and represent a total of seven Tb^{3+} ions also perhaps associated with the five amphipathic helices that jut into the cytoplasm and/or the cytoplasmic 67–100 amino acids of each subunit that are not present in the 4 Å model. In the desensitized state these clusters represent a total of only three to four Tb^{3+}

ions. The total decrease in Tb^{3+}/AChR in the desensitized state compared with the closed resting state is ~18 ± 7.5 Tb^{3+} ions.

DISCUSSION

Analysis of the current refinement scheme compared with previous scheme

The previous heavy atom refinement (7) was carried out only on the data collected from AChR enriched membranes in the absence of carbamylcholine, and the analysis was modeled after the crystallographic heavy atom refinement scheme of Dickerson et al. (20), modified to handle continuous small-angle x-ray diffraction data rather than crystallographic reflections. A refinement window of 150 Å was used, and the six ''clusters'' initially identified in the Fourier difference map were refined. Attempts to refine the positions, amplitudes, and *B*-factors simultaneously of these six clusters did not converge. As a result the *B*-factors of the clusters were fixed at values obtained from previous refinements using smaller numbers of clusters. Then the positions and amplitudes of the six clusters were simultaneously refined with the fixed *B*-factors to obtain the lowest *R*-factor refined solution. The quantitative analysis of the refined anomalous x-ray signal at $s = 0.0\ Å^{-1}$ of $F_{o\text{-}7505}(s) - F_{o\text{-}7515}(s)$, as well as a Tb^{3+} titration of the membranes yielded 45 Tb^{3+}/AChR. In Fairclough et al. (7) the membrane electron density profile was mistakenly reversed relative to the refined Tb distributions in Figs. 4 and 5. In the new refinement we have rectified these glitches.

With the enhanced data storage capabilities and the increased speed of individual personal computer processors currently available, we have exploited these capabilities with the refinement procedure used in the current studies. Both methods use exactly the same calculation to measure ''goodness of fit'' between solution and data, and both methods attempt to find a minimum *R*-factor in the solution space. The fundamental difference between the two methods is the degree to which the solution space is explored. Because of the limited computing power in 1983 and 1984, the original refinement used a derivative of the Dickerson et al. (20) method for finding a minimum *R*-factor in the solution space. The method used in this publication explores the solution space to a much greater extent due to many orders of magnitude increase in computing power. The new scheme overcomes some of the limitations imposed by the previous scheme. The 150 Å window used in the previous refinement was unable to predict the bifurcated peak at 0.02 $Å^{-1}$ in the anomalous difference ''wave'' collected for the carbamylcholine treated membranes (Fig. 5 *b*). However, expanding the window to 220 Å did enable us to predict the bifurcation of the first peak seen at 0.02 $Å^{-1}$ in the ΔF data of Fig. 5 *b*. The current refinement scheme enables us to skirt the previous refinement's convergence problem. These two factors together enable us to lower the *R*-factor from ~0.5 to ~0.2. We also get a sense of the statistics of the differences from the mean of Tb^{3+} density in each cluster with the model's corresponding fits and *R*-factors of the diffraction data. These statistics are much harder to extract from the prior least squares minimization procedure. The choice of 45 Gaussians is not critical because we also refine the *A* factor. For example in the +carbamylcholine refinement, we find only 27 Tb^{3+} ions even though we start with 45 Gaussians.

What is learned about the AChR from this study?

Overall considerations

We find that at 50 μM, Tb^{3+} preferentially binds to the protein rather than to the lipid bilayer phosphate headgroups. This may be the result of low density of lipids in the AChR-enriched membranes preventing enough phosphates from chelating the Tb^{3+} with its high coordination number of 6–8, or the [Tb^{3+}] is too low to effectively complex with the low density of headgroups, or alternatively, a small amount of Tb^{3+} does bind, but it is in the noise level of the experiment. We find the refinement procedure applied to both ± carbamylcholine data sets, results in roughly similar Tb^{3+} ion distributions, but with some 18 fewer Tb^{3+} ions associated with the AChR in the desensitized state. This is very close to the decrease in Tb^{3+} binding to carbamylcholine treated AChR enriched membranes compared with untreated membranes observed with the spectral Tb^{3+} titrations. Interestingly, the groups of Tb^{3+} at the levels marking the ends of the cation selective pore (peaks 3,4 and 6,7), rearrange positions rather than lose Tb^{3+} stoichiometry as the AChR converts between the closed resting and closed desensitized states. However, the three major clusters in peaks 2, 5, and 9 in Figs. 7 and 8 each seem to bind only half as many Tb^{3+} ions when the AChR converts from the closed resting to the closed desensitized state accounting for 10 of the 18 Tb^{3+} ion difference between the two states. This loss of ionic interactions in the presence of the agonist is reminiscent of the transition between the taut state of Hb with a considerable number of salt bridges in the deoxygenated state that are abolished in the liganded, O_2-bound, oxygenated state (21,22).

Specific Tb^{3+} sites in the AChR extracellular domain

In Fig. 8 we propose the CPK formatted, chelating-O-containing, amino acid side chains and/or carbonyl O as anchors of Ca^{2+}/Tb^{3+} binding sites with the green spheres centered between the O illustrating the proposed location of these ions in the 4 Å model (19). The orange space filling amino acids in Fig. 8 are γN67, δN70, and δN208 that are the attachment sites for complex oligosaccharides (23,24). These are a heterogeneous group of sialylated bi-, tri-, and tetra-antennary oligosaccharides (25) that are potential anchors for the Tb^{3+} density in peak 1 some 20–30 Å above the AChR extracellular domain. This is consistent with the 17 Å extension of the shorter N-linked carbohydrate of *Erthrina corallodendron* lectin seen in its crystal structure

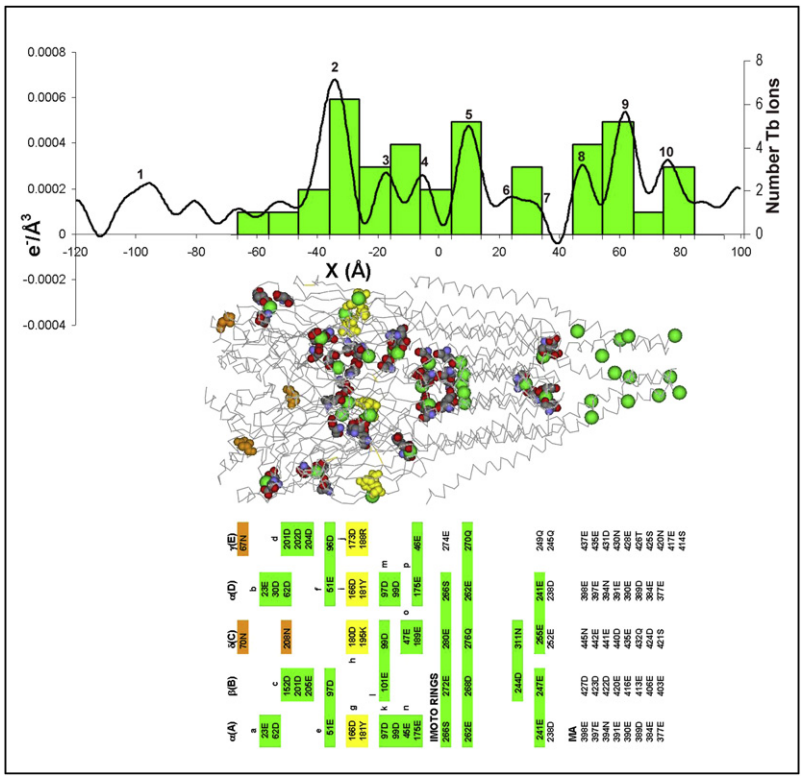

FIGURE 8 A comparison of the Tb^{3+} distribution (*line in the graph*) in the closed resting state of the AChR from Fig. 7 (Arabic numerals above the peaks are those listed in Table 2) with a map (*green histogram on the graph*) of potential bound Tb^{3+} ions (*green spheres*) placed on the 4 Å model of the AChR selected by structural homology to the Ca^{2+} sites on the acetylcholine binding protein (*yellow side chains* and *boxes*), as well as by pairs of carboxylate side chains (CPK format) in the 3D model located in close proximity to one another with a *Z* coordinate near a peak of Tb^{3+} density in the distribution. The model is oriented such that an α subunit (*A*) is at the bottom of the figure as viewed, the orange space-filling side chain to the left and just above the A subunit is that of the γ subunit, and the other two orange side chains are from the δ subunit. The Tb^{3+} ions placed in the model are binned in 10 Å groups and this distribution is displayed in the histogram overlaid on the Tb^{3+} distribution graph. The side chains of the subunit sequence numbers followed by the amino acid one letter code selected for Tb^{3+} chelating partners are indicated as pairs in green boxes in the side-wise table at the bottom of the figure, and the position of the boxes roughly correlates with the *Z* coordinate location of the sites on the model. The orange colored side chains are the AChR asparagines to which complex oligosaccharides are attached that provide sialic acid clusters to potentially chelate Tb^{3+} ions to the left of the protein head of the AChR model.

(26). Given the heterogeneity of the AChR complex oligosaccharides, their electron density compared with water, and their potential crystallographic disorder, they are not apparent in the electron density of Fig. 7 to the left of the protein density of the AChR extracellular domain. The 1.8 Tb^{3+}/AChR difference in stoichiometry in this group ±carbamylcholine is difficult to rationalize in terms of the two states of the AChR studied, but seems just a bit larger than the noise level of the experiment (±0.7 Tb^{3+}/AChR for this peak from Table 2). Another consideration for the carbamylcholine-induced changes of the Tb^{3+} density in this peak is that the five best refinement solutions of Fig. 6 *a* in the region –110 Å $< X <$ −60 Å individually differ from one another more than those of the five best solutions of Tb^{3+} density in the carbamylcholine treated sample of Fig. 6 *b*. By both criteria carbamylcholine seems to exert an effect on this group of bound Tb^{3+} ions.

In Fig. 8 the proposed locations of the other Tb^{3+} ions along the central axis (normal to the membrane), *X*, are placed between pairs of COO^- side chains and/or carbonyl O in close proximity to one another in the refined AChR structure. These sites are binned in 10 Å groups along *X*, the normal to the bilayer, and the distribution of Tb^{3+} in these bins is presented as the bar graph in Fig. 8 for comparison with the distribution of Tb^{3+} we determined experimentally with the AChR in the closed resting state. The proposed chelating amino acids are listed in the table at the bottom of Fig. 8 as pairs in green/yellow boxes roughly according to their location in the model along the *x* axis.

The proposed chelating amino acids highlighted in yellow deserve special mention. These are the amino acids of the *Torpedo* α(A), γ(E), and δ(C) subunits homologous to the amino acids of the ACh-binding protein (5) in contact with bound Ca^{2+} ions in that crystal structure (see sequence and structural alignment in Fig. S5). These are also homologous to the amino acids implicated in the Ca^{2+} potentiation of the α7 and the α7-5HT_3 chimera receptor Na^+ currents (3). In both closed states of the AChR studied in this study, we find at least four to five Tb^{3+} located at this position along the central axis. The C_α structural homology in this region between the binding protein and the *Torpedo* subunits is evident (Fig. S5) despite differences in the side-chain orientations in the proposed structure (19), and strongly suggests Ca^{2+} sites at these positions (Fig. 8, *g–j*, and Fig. S3) even though the side chains in the refined AChR structure are not congruent with those in the binding protein structure. In addition we have included five additional Tb^{3+} sites at this level (Fig. 8, *e*, *f*, *k*, *l*, and *m*, and Fig. S3) that may form from pairs of aspartate and glutamate side-chains on the inner face of the AChR vestibule raising the total at this level to the nine Tb^{3+} ions detected in peak 2 in the closed resting state. Whether carbamylcholine causes differential Tb^{3+} binding to sites on the inside or on the outside wall of the synaptic head, or from a mixture of these sites at this level, our data do not allow us to decide, but there is a decrease of four to five Tb/AChR at this level in the desensitized state compared with that in the closed resting state.

Interface of the extracellular with the TM domain and in the TM domain

The Tb^{3+} ions in peaks 3 and 4 of Figs. 7 and 8 (Fig. 8, *n–p*, and Fig. S3) potentially are anchored by pairs of COO^- side chains: (αE45, αE175), (δE47, δE189), and (αE175, γE46). These Tb^{3+} ions along with those potentially anchored in the closed resting state with the polar and COO^- side chains from the extracellular Imoto ring (8): αS266, βE272, δE280, αS266, and γE274 featured in the transmembrane domain presented in Fig. S4 stereo pairs would seem to mark interesting Ca^{2+} sites stabilizing the closed state of the ion channel pore. It is in this region of the AChR where the Tb^{3+} ion distribution changes between the closed resting state and the carbamylcholine desensitized state without changing Tb^{3+} stoichiometry.

Next the Tb^{3+} in peak 5 of Figs. 7 and 8 is just to the cytoplasmic side of the Imoto (8) intermediate ring of carboxylates presented in Fig. 8 and Fig. S4. Apart from the three carboxylates in the intermediate ring, no other negatively charged components from the protein or fatty acid chains are available to balance the total +15 charge from the five Tb^{3+} ions in this cluster. Because this cluster refines in both samples, we believe this is strong evidence in support of a membrane component other than the protein or bilayer holding multivalent cations in this cluster. The Unwin 4Å AChR structure (19) is refined with only the AChR subunit polypeptides threaded through the electron density, so no cations or lipids are present in the model. However, Hamouda et al. (27) report the importance of five tightly associated phosphatidic acids/AChR in membrane reconstituted AChR function, which lipids potentially could provide some charge balance to the five Tb^{3+} ions we detect in this most striking cluster of the closed resting state of the AChR. In support of this is the prominent shoulder of electron density at 20 Å in the membrane profile (Fig. 7, *red curve*) that could be evidence of a cluster of phosphate groups from phosphatidic acid poking their heads into the water-filled pore at this level with the fatty acid chains intercalated in the hydrophobic protein core of the transmembrane domain. The Imoto ring closest to the cytoplasm is in a position to bind the three Tb^{3+} ions we find in peaks 6 and 7 in Figs. 7 and 8. In scanning the 4 Å model for potential nests for Tb^{3+} sites, we find sites between αE241 and βE247, βD244 and δN311, and δE255 and αE241. Because both the resting state and the desensitized state are closed states, we are unable to tell whether these sites in the pore are occupied in the open channel state. The presence of these multivalent cations suggests a potential role in stabilizing the closed states if not by directly blocking the pore, then by stabilizing the helical components forming the lining of the pore at these locations, and sealing the pore of the Unwin closed state model. We are attempting to see if Tb^{3+} is able to alter the gating kinetics of the ion channel by either prolonging the mean closed time intervals in single channel recordings, or just decreasing the whole cell current in oocytes expressing the AChR much as Mg^{2+} was found to perturb the AChR single channel currents (8).

The cytoplasmic domain

The three Tb^{3+} groups located in peaks 8, 9, and 10 of Figs. 7 and 8 lie in the region of the cytoplasmic amphipathic helices in the 4 Å model. However, the absence of significant portions of cytoplasmic structural elements from the 4 Å model reduces the reliability of the positioning of these sites, so we have only indicated sites on the amphipathic helices. These sites are most likely unfilled under physiological conditions because of the low [Ca^{2+}] inside the cell. When the channel opens allowing some Ca^{2+} to enter the cell, it is possible the elevated [Ca^{2+}] enables Ca^{2+} to bind to these sites helping to ''re-close the open channel'' although the functional effect of mutating the *E* and *D* residues of the α subunit amphipathic helix to *K* singly on the measured conductance of the mutated channels is minimal (8). Interestingly, in our experiments carbamylcholine wreaks havoc on the location and stoichiometric Tb^{3+}/AChR ratios for these three sites (compare the region from 40–90 Å in Fig. 6, *a* and *b*). In the closed resting state these three sites refine relatively reliably. However, in the presence of carbamylcholine the total stoichiometry of 13+ is reduced to ~6.5 with considerable variability in the five best refinement positions and stoichiometry.

CONCLUSION

All the modeled sites are indicated in Fig. 8 for the closed resting state with varying levels of confidence, but in total they provide a plausible rationale for the Tb^{3+} distribution we measure in Fig. 7. Considering the resolution and the missing pieces of the 4 Å model, the agreement between the distributions seen in the Fig. 8 bar graph and the Tb^{3+} distribution seems reasonable. Because the model protein coordinates are determined by refinement of the protein sequences in the electron density maps at 4 Å resolution, the side-chains of the model may be displaced from their optimal chelating orientation. The magnitude and the location of the changes of the Tb^{3+} distribution between the closed resting and desensitized states of the AChR point to a likely role for multivalent cations in stabilizing various functional states of the AChR, and a likely role for them in channel gating mechanics.

SUPPORTING MATERIAL

Five figures are available at http://www.biophysj.org/biophysj/supplemental/S0006-3495(09)00416-0.

Note added in proof: An unusual nonbilayer phosphatidic acid is predicted by Dickey and Faller (28) in the presence of the AChR transmembrane helices.

R.H.F. thanks Keith O. Hodgson and Robert M. Stroud for providing him the opportunity to study the role of multivalent cations in AChR function, and he thanks his many collaborators at the Stanford Synchrotron Radiation Lab who made the collection and analysis of the small-angle x-ray data possible.

Included in this group of investigators is Richard Miake-Lye, the designer of the small-angle camera and data collection and reduction system that was upgraded by Stevan Hubbard, Soichi Wakatski, and Jean-Luc Ranck. R.H.F also thanks the reviewers of this work who contributed significant improvements to the presentation and analysis of the anomalous scattering data, and gratefully acknowledges the critical reading of the manuscript by, and suggestions from, Drs. David P. Richman, Tsung-Yu Chen, and Robert M. Stroud. Funding for this work has come from the tireless energy of Keith O. Hodgson in securing the National Institutes of Health biotechnology resource program for support of the biological applications of synchrotron radiation and the Department of Energy for the support of SSRL.

This work was funded partially by a grant from the Myasthenia Gravis Foundation of California.

REFERENCES

1. Sine, S. M., T. Claudio, and F. J. Sigworth. 1990. Activation of *Torpedo* acetylcholine receptors expressed in mouse fibroblasts. Single channel current kinetics reveal distinct agonist binding affinities. *J. Gen. Physiol.* 96:395–437.
2. Decker, E. R., and J. A. Dani. 1990. Calcium permeability of the nicotinic acetylcholine receptor: the single-channel calcium influx is significant. *J. Neurosci.* 10:3413–3420.
3. Galzi, J. L., S. Bertrand, P. J. Corringer, J. P. Changeux, and D. Bertrand. 1996. Identification of calcium binding sites that regulate potentiation of a neuronal nicotinic acetylcholine receptor. *EMBO J.* 15:5824–5832.
4. Czajkowski, C., and A. Karlin. 1995. Structure of the nicotinic receptor acetylcholine-binding site. Identification of acidic residues in the delta subunit within 0.9 nm of the alpha subunit-binding site. *J. Biol. Chem.* 270:3160–3164.
5. Brejc, K., W. J. van Dijk, R. V. Klaassen, M. Schuurmans, J. van der Oost, et al. 2001. Crystal structure of an ACh-binding protein reveals the ligand-binding domain of nicotinic receptors. *Nature*. 411:269–276.
6. Chang, H. W., and E. Neumann. 1976. Dynamic properties of isolated acetylcholine receptor proteins: Release of calcium ions caused by acetylcholine binding. *Proc. Natl. Acad. Sci. USA*. 73:3364–3368.
7. Fairclough, R. H., R. C. Miake-Lye, R. M. Stroud, K. O. Hodgson, and S. Doniach. 1986. Location of terbium binding sites on acetylcholine receptor-enriched membranes. *J. Mol. Biol.* 189:673–680.
8. Imoto, K., C. Busch, B. Sakmann, M. Mishina, T. Konno, et al. 1988. Rings of negatively charged amino acids determine the acetylcholine receptor channel conductance. *Nature*. 335:645–648.
9. Wilson, G., and A. Karlin. 2001. Acetylcholine receptor channel structure in the resting, open, and desensitized states probed with the substituted-cysteine-accessibility method. *Proc. Natl. Acad. Sci. USA*. 98:1241–1248.
10. Neubig, R. R., E. K. Krodel, N. D. Boyd, and J. B. Cohen. 1979. Acetylcholine and local anesthetic binding to *Torpedo* nicotinic postsynaptic membranes after removal of nonreceptor peptides. *Proc. Natl. Acad. Sci. USA*. 76:690–694.
11. Barela, T. D., and A. D. Sherry. 1976. A simple, one-step fluorometric method for the determination of nanomolar concentrations of terbium. *Anal. Biochem.* 71:351–357.
12. Ross, M. J., M. W. Klymkowsky, D. A. Agard, and R. M. Stroud. 1977. Structural studies of a membrane-bound acetylcholine receptor from *Torpedo Californica*. *J. Mol. Biol.* 116:635–659.
13. Gabriel, A. 1977. Position sensitive x-ray detector. *Rev. Sci. Instrum.* 48:1303–1305.
14. Miake-Lye, R.C. 1983. Anomalous x-ray Scattering as a probe of biological structure. PhD thesis. Stanford University, Stanford, California.
15. Miake-Lye, R. C., S. Doniach, and K. O. Hodgson. 1983. Anomalous x-ray scattering from terbium-labeled parvalbumin in solution. *Biophys. J.* 41:287–292.
16. Klymkowsky, M. W., and R. M. Stroud. 1979. Immunospecific identification and three-dimensional structure of a membrane-bound acetylcholine receptor from *Torpedo californica*. *J. Mol. Biol.* 128:319–334.
17. Unwin, N., C. Toyoshima, and E. Kubalek. 1988. Arrangement of the acetylcholine receptor subunits in the resting and desensitized states, determined by cryoelectron microscopy of crystallized *Torpedo* postsynaptic membranes. *J. Cell Biol.* 107:1123–1138.
18. Stroud, R. M., and D. A. Agard. 1979. Structure determination of asymmetric membrane profiles using an iterative Fourier method. *Biophys. J.* 25:495–512.
19. Unwin, N. 2005. Refined structure of the nicotinic acetylcholine receptor at 4A resolution. *J. Mol. Biol.* 346:967–989.
20. Dickerson, R. E., J. E. Weinzierl, and R. A. Palmer. 1968. A least-squares refinement method for isomorphous replacement. *Acta Crystallogr.* B24:997–1003.
21. Perutz, M. 1970. Haem-Haem interaction and the problem of allostery. *Nature*. 228:726–734.
22. Bettati, S., A. Mozzarelli, and M. F. Perutz. 1998. Allosteric mechanism of hemoglobin: rupture of salt-bridges raises the oxygen affinity of the T-structure. *J. Mol. Biol.* 281:581–585.
23. Poulter, L., J. P. Earnest, R. M. Stroud, and A. L. Burlingame. 1989. Structure, oligosaccharide structures, and posttranslationally modified sites of the nicotinic acetylcholine receptor. *Proc. Natl. Acad. Sci. USA*. 86:6645–6649.
24. Strecker, A., P. Franke, C. Weise, and F. Hucho. 1994. All potential glycolsylation sites of the nicotinic acetylcholine receptor δ subunit from *Torpedo californica* are utilized. *Eur. J. Biochem.* 220:1005–1011.
25. Shoji, H., N. Takahashi, H. Nomoto, M. Ishikawa, I. Shimada, et al. 1992. Detailed structural analysis of asparagine-linked oligosaccharides of the nicotinic acetylcholine receptor from *Torpedo californica*. *Eur. J. Biochem.* 207:631–641.
26. Shaanan, B., H. Lis, and N. Sharon. 1991. Structure of a legume lectin with an ordered N-linked carbohydrate in complex with lactose. *Science*. 254:862–866.
27. Hamouda, A. K., D. Sauls, N. Vardanyan, M. Sanghvi, and M. P. Blanton. 2005. Assessing the lipid requirements of the nicotinic acetylcholine receptor. *Biophys. J.* 88:624a (Abstr).
28. Dickey, A. N., and R. Faller. 2008. Behavioral difference between phosphatidic acid and phosphatidylcholine in the presence of the nicotinic acetylcholine receptor. *Biophys. J.* 95:5637–5647.